Publications of the Astronomical Society of the Pacific, **119**: 1308–1324, 2007 November

Refinement of the *Spitzer Space Telescope* Pointing History Based on Image Registration Corrections from Multiple Data Channels

Howard L. McCallon,[1] John W. Fowler,[1] Russ R. Laher,[2] Frank J. Masci,[1] and Mehrdad Moshir[3]
Received 2007 June 27; accepted 2007 September 12; published 2007 December 3

ABSTRACT. Position reconstruction for images acquired by the Infrared Array Camera (IRAC), one of the science instruments onboard the *Spitzer Space Telescope*, is a multistep procedure that is part of the routine processing done at the Spitzer Science Center (SSC). The IRAC instrument simultaneously images two different sky footprints, each with two independent infrared passbands (channels). The accuracy of the initial *Spitzer* pointing reconstruction is typically slightly better than 1″. The well-known technique of position matching imaged point sources to even more accurate star catalogs to refine the pointing further is implemented for SSC processing of IRAC data as well. Beyond that, the optimal processing of redundant pointing information from multiple instrument channels to yield an even better solution is also performed at the SSC. Our multichannel data processing approach is particularly beneficial when the star-catalog matches are sparse in one channel but copious in others. A thorough review of the algorithm as implemented for the *Spitzer* mission reveals that the mathematical formalism can be fairly easily generalized for application to other astronomy missions. The computation of pointing uncertainties, the interpolation of pointing corrections and their uncertainties between measurements, and the estimation of random-walk deviations from linearity are special areas of importance when implementing the method. After performing the operations described in this paper on the initial *Spitzer* pointing, the uncertainty in the observatory pointing history file is reduced 10–15 fold.

1. INTRODUCTION

During the collection of imaging data, the *Spitzer Space Telescope* makes considerable use of overlapping images arranged in a raster pattern, a very common mode of astronomical data acquisition. This involves steady pointing of imaging arrays on each node in a grid of sky positions such that individual fields of view can be assembled into a mosaic. The construction of a mosaic profits from accurate knowledge of the individual image positions, since image registration error causes blurring of point sources in overlap regions when the images are combined. Fortunately, *Spitzer*'s pointing accuracy is better than 1″ (Werner et al. 2004), and this gives a very good zeroth-order solution that forms the basis for further pointing refinement. The absolute accuracy is determined by limitations in telescope pointing control, tracking sensors, and thermomechanical disturbances. Masci et al. (2004, hereafter Paper I) described the improvement of *Spitzer* image registration by matching point sources detected in image overlap regions and globally minimizing source position discrepancies over an entire set of images acquired by *Spitzer*'s Infrared Array Camera (IRAC). The method further made use of point-source matches to the Two Micron All Sky Survey (2MASS) catalog, which has an astrometric accuracy of order 100 milliarcseconds (mas; Skrutskie et al. 2006). This processing produces a list of corrections in right ascension, declination, and twist angle (rotation about the telescope's optical axis) for the individual images in a mosaic. Experience has shown that the positions of all images are usually improved, but occasionally a lack of usable point sources will leave an image without corrections. The success rate of the method was characterized more completely in a later statistical study, Laher et al. (2006), based on a much larger IRAC data set than that discussed in Paper I.

The effectiveness of the pointing refinement increases with the number of usable point sources in overlapping regions, and because detectable stellar spectra tend to peak at visual wavelengths, this number tends to be significantly higher in the shorter wavelength IRAC channels. The four infrared-wavelength channels take data simultaneously and correspond to four independent focal plane arrays with passband filters centered at 3.6, 4.5, 5.8, and 8.0 μm, however, and so the information used to refine the pointing estimates in the shorter wavelengths can also contribute to refining the longer ones by mapping it through the geometrical

[1] Infrared Processing and Analysis Center, California Institute of Technology, Pasadena, CA 91125; laher@ipac.caltech.edu.
[2] Spitzer Science Center, California Institute of Technology, Pasadena, CA 91125.
[3] Jet Propulsion Laboratory, 4800 Oak Grove Drive, Pasadena, CA 91109.

relationships between channels. Furthermore, the continual improvement in instrument calibration and data reduction techniques results in several reprocessing runs for all *Spitzer* observations. It was decided, therefore, to use all the available information to compute a channel-independent position determination, which could then be applied to all four channels by refining the telescope boresight pointing history file (BPHF) itself. The result has been dubbed the "super" boresight pointing history file (SBPHF).

The BPHF is a time-tagged list of the telescope boresight's right ascension and declination, the twist angle of the focal plane, and certain auxiliary parameters sampled at 2 Hz. It originates onboard the spacecraft, where attitude sensors are used by the control software to compute these angles and record associated quantities such as gyro outputs, star sensor information, etc. After downlinking the pointing data, the values are processed and reformatted at the Jet Propulsion Laboratory and then sent to the Spitzer Science Center (Bayard et al. 2003). For a given observation, the BPHF records covering the observation time are used to compute averaged celestial coordinates for that instrument's field of view by employing the geometrical relationship between that instrument array's coordinate system and that of the telescope boresight and focal plane. This relationship is represented in terms of Euler angles in the telescope focal plane system. The Euler angles are used to compute a rotation matrix that can be applied to the telescope's International Celestial Coordinate System (ICRS) coordinates to obtain the ICRS coordinates of the instrument. This is done for all of the 2 Hz samples during the observation, and averaging in the vector domain is used to compute the mean and standard deviation of each of the active instruments' celestial coordinates.

The BPHF-derived instrument-frame coordinates are then refined as described in Paper I, and the set of corrections for a complete multichannel mosaic are then used to transform the BPHF values into improved pointing results, which are then saved in the SBPHF. The process of computing the SBPHF involves mapping the image coordinate corrections through the Euler angles to the telescope system and shifting the original coordinates by a slowly varying amount to null out the mean pointing errors over the 2 Hz samples. These corrections sample the pointing error only on timescales of typical observations (commonly 10 s or longer); this is equivalent to high-pass filtering of pointing jitter (which can be seen as the fine structure in the trajectories shown in Fig. 4). The high-frequency content of pointing jitter (at frequencies greater than $\sim$0.1 Hz) is unaffected by our processing, and therefore, the SBPHF retains the BPHF control-system jitter while yielding the refined image coordinates when used in place of the BPHF. Once the SBPHF has been computed, it can be used instead of the BPHF on any subsequent reprocessing, and since it implicitly contains the refinement information from all channels, the longer wavelengths also benefit fully. It should be noted that this goal could be achieved in a variety of ways, and the one described herein was designed to fit into the existing data-processing pipeline architecture already implemented at the Spitzer Science Center.

The purpose of this paper is to present our multichannel data-fusion algorithm for augmenting the processing described in Paper I. In order to achieve even greater pointing accuracy and lead to the generation of the aforementioned SBPHF. The required input data for the algorithm, along with nomenclature, are described in § 2. The full mathematical description of the algorithm itself is given in § 3. Our discussion and conclusions wrap up this paper in § 4. Extensive additional details on uncertainty interpolation, random-walk calibration, and restoring orthonormality to the transformation matrix are included in Appendices A–C.

2. INPUT DATA

Four types of input data are needed for our multichannel algorithm that computes the SBPHF: (1) instrument field of view (FOV) data, (2) refined pointing measurement data, (3) BPHF data, and (4) processing control data. Each of these data sets and their nomenclature, reference frames, etc., are described in separate subsections below. For brevity, we take the refined pointing measurement data and BPHF data to have been segmented into ensembles corresponding to single-channel mosaics and then describe the processing applicable to one such mosaic.

2.1. Instrument FOV Data

The Cartesian coordinate system of the *Spitzer Space Telescope* is defined with the x-axis pointing out along the optical boresight, which is perpendicular to the telescope's focal plane. Its z-axis is defined by hardware fiducial marks in the telescope's focal plane that point toward *Spitzer*'s Sun shield. The corresponding y-axis completes the right-handed system. When mapped onto the sky with the boresight on the north celestial pole and the z-axis pointing to the vernal equinox, by definition, the right ascension is zero, and the declination and twist angle are both 90°.

The four IRAC instrument arrays, one for each of the four IRAC data channels, employ two apertures in the telescope's focal plane whose centers are offset from the telescope's boresight as shown in Figure 1, which also shows the apertures of the other science instruments onboard the *Spitzer Space Telescope*. The coordinate systems of the instrument arrays are each separately related to the telescope's coordinate system by a coordinate-system rotation characterized by three Euler angles. Table 1 gives the set of Euler angles for each of the four IRAC channels.

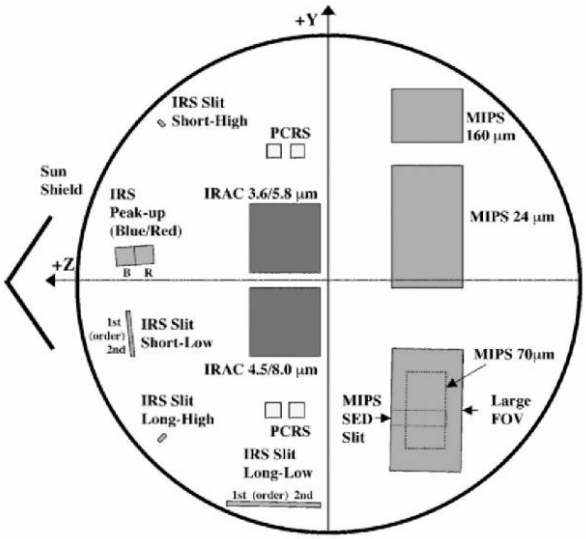

Fig. 1.—Focal plane layout of the *Spitzer Space Telescope*. The telescope boresight is located at the coordinate-system origin. (From http://ssc.spitzer.caltech.edu/documents/Spitzer_PocketGuide.pdf.)

Thus, each instrument array has a coordinate system similar to the telescope's, with the x-axis being the FOV boresight from the center of the array and the z-axis pointing parallel to the rows of the array in the direction nearest to the telescope z-axis. The relationship to the telescope system is defined by angles denoted θ_1, θ_2, and γ_I. The first two angles account for the off-axis focal-plane location of the center of the instrument array, and the third accounts for the rotational alignment about its FOV boresight relative to the telescope focal-plane coordinates. Starting in the telescope system, the following rotations lead to the instrument system: θ_1 about Z, θ_2 about Y, and γ_I about X. The rotation matrices are

$$\begin{pmatrix} 1 & 0 & 0 \\ 0 & \cos\gamma_I & \sin\gamma_I \\ 0 & -\sin\gamma_I & \cos\gamma_I \end{pmatrix} \begin{pmatrix} \cos\theta_2 & 0 & -\sin\theta_2 \\ 0 & 1 & 0 \\ \sin\theta_2 & 0 & \cos\theta_2 \end{pmatrix} \begin{pmatrix} \cos\theta_1 & \sin\theta_1 & 0 \\ -\sin\theta_1 & \cos\theta_1 & 0 \\ 0 & 0 & 1 \end{pmatrix}.$$

Multiplying these in the order shown yields the rotation matrix T_B^I for converting BPHF coordinates to instrument coordinates, where the labels B and I indicate the BPHF and instrument systems, respectively. Since these are orthonormal matrices, the inverse T_I^B is just the transpose of T_B^I. It is T_I^B that are needed below,

$$T_I^B = \begin{pmatrix} \cos\theta_1\cos\theta_2 & -\sin\theta_1\cos\gamma_I + \cos\theta_1\sin\theta_2\sin\gamma_I & \sin\theta_1\sin\gamma_I + \cos\theta_1\sin\theta_2\cos\gamma_I \\ \sin\theta_1\cos\theta_2 & \cos\theta_1\cos\gamma_I + \sin\theta_1\sin\theta_2\sin\gamma_I & -\cos\theta_1\sin\gamma_I + \sin\theta_1\sin\theta_2\cos\gamma_I \\ -\sin\theta_2 & \cos\theta_2\sin\gamma_I & \cos\theta_2\cos\gamma_I \end{pmatrix}. \quad (1)$$

The FOV data include uncertainties for each of the three angles, along with a correlated-error parameter for the first two. The parameters are summarized as follows.

TABLE 1
FOV Angles and Uncertainties for the *Spitzer* IRAC

IRAC Channel	θ_1 (deg)	θ_2 (deg)	γ_I (deg)	$\sigma(\theta_1)$ (arcsec)	$\sigma(\theta_2)$ (arcsec)	Co-Sigma (θ_1, θ_2) (arcsec)	$\sigma(\gamma_I)$ (arcsec)
1	−0.062291	0.047675	359.457688	0.1	0.1	0.0	0.1
2	−0.060112	0.047388	359.698891	0.1	0.1	0.0	0.1
3	0.050812	0.045344	359.279852	0.1	0.1	0.0	0.1
4	0.051131	0.045863	170.969369	0.1	0.1	0.0	0.1

θ_1—First Euler angle, about Z.
θ_2—Second Euler angle, about Y.
γ_I—Third Euler angle, about X.
σ_{θ_1}—1 σ uncertainty in θ_1.
σ_{θ_2}—1 σ uncertainty in θ_2.
σ_{γ_I}—1 σ uncertainty in γ_I.
$\sigma_{\theta_1\theta_2}$—Co-sigma defining correlation in θ_1 and θ_2 uncertainties.

The "co-sigma" parameter contains the error covariance information for the first and second Euler angles; it may be positive or negative, according to the correlation. For human readability, the uncertainty parameters are maintained in the same units as the parameters they describe, i.e., standard-deviation units rather than variance units. The diagonal elements of error covariance matrices are obtained by squaring the 1 σ uncertainties; off-diagonal elements are obtained by multiplying the co-sigma value by its absolute value. Missing co-sigma parameters correspond to negligible correlations taken to be zero. The values of these parameters for the four IRAC channels are given in Table 1. Although the co-sigma parameters are all zero at present, they continue to be taken into account in order to accommodate the possibility that future calibrations may provide values for them. It should be noted that the processing described in this paper can be expanded to estimate all of the parameters defined in this section; at this time, however, since the current accuracy of these parameters is well within the requirements, the *Spitzer* project considers this broadened scope to be of relatively low priority.

2.2. Refined Pointing Measurement Data

The refined pointing measurement data consist of a set of records for instrument frames spanning the mosaic spatially, temporally, and across the four IRAC data channels. Each record corresponds to an image whose analysis yielded corrections to its celestial coordinates as described in Paper I. Values for the following parameters constitute each record, where the subscript M denotes a "measurement" quantity to distinguish it from a BPHF quantity below.

α_M—Refined right ascension.
δ_M—Refined declination.
γ_M—Refined twist angle.
$\Delta\alpha_M$—Correction to unrefined right ascension.
$\Delta\delta_M$—Correction to unrefined declination.
$\Delta\gamma_M$—Correction to unrefined twist angle.
T_M—Time tag.
σ_{α_M}—1 σ uncertainty in $\Delta\alpha_M$.
σ_{δ_M}—1 σ uncertainty in $\Delta\delta_M$.
σ_{γ_M}—1 σ uncertainty in $\Delta\gamma_M$.
$\sigma_{\alpha\delta_M}$—Co-sigma defining correlation in $\Delta\alpha_M$ and $\Delta\delta_M$ uncertainties.
N_C—IRAC wavelength channel number (1–4).

Given the axis definitions in § 2.1 above, the Euler angle sequence to achieve an instrument orientation corresponding to a given image is $\alpha_M - 90°$ about X, $\delta_M - 90°$ about Z, and γ_M about X. Note that right ascension and declination are the same angles typically found in astronomical FITS headers specified by the keywords CRVAL1 and CRVAL2. The twist angle herein, however, is a true Euler angle, unlike the left-handed east-of-north angle, which is commonly called the "position angle" and related to twist by P.A. $= 90° -$ twist.

Setting up each rotation matrix and multiplying them as in § 2.1 yields the transformation matrix T_C^I for converting any vector in celestial coordinates to the instrument coordinate system, where C indicates the celestial coordinates of an arbitrary vector, expressed below in terms of the instrument array coordinates for this measurement,

$$T_C^I = \begin{pmatrix} \sin\delta_M & -\sin\alpha_M\cos\delta_M & \cos\alpha_M\cos\delta_M \\ \cos\delta_M\cos\gamma_M & \sin\alpha_M\sin\delta_M\cos\gamma_M + \cos\alpha_M\sin\gamma_M & -\cos\alpha_M\sin\delta_M\cos\gamma_M + \sin\alpha_M\sin\gamma_M \\ -\cos\delta_M\sin\gamma_M & -\sin\alpha_M\sin\delta_M\sin\gamma_M + \cos\alpha_M\cos\gamma_M & \cos\alpha_M\sin\delta_M\sin\gamma_M + \sin\alpha_M\cos\gamma_M \end{pmatrix}. \quad (2)$$

2.3. BPHF Data

The BPHF data include the following parameters sampled at 2 Hz:

α_B—Right ascension.
δ_B—Declination.
γ_B—Twist angle.
T_B—Time tag.
σ_{α_B}—1 σ uncertainty in α_B.
σ_{δ_B}—1 σ uncertainty in δ_B.
σ_{γ_B}—1 σ uncertainty in γ_B.
$\sigma_{\alpha\delta_B}$—Co-sigma defining correlation in α and δ uncertainties.

The matrix T_C^B, which transforms a vector from the celestial coordinate system directly to the telescope coordinate system, can be written down in the same form as equation (2), but with (α_B, δ_B, γ_B) substituted for (α_M, δ_M, γ_M), respectively. This gives the explicit dependence on the BPHF telescope-pointing parameters and is one of the relationships needed to derive equation (3) below. In addition, since T_C^I transforms a vector to the instrument system, and T_I^B transforms a vector in that system to the telescope coordinate system, the matrix that transforms a vector to the telescope coordinate system is also given by $T_C^B = T_I^B T_C^I$. This matrix explicitly contains the dependence of the telescope coordinate system on all of the instrument parameters, and so this is what is used below to compute the mapping matrix that connects instrument position and uncertainty information to the telescope system.

The Cartesian system represented by any matrix defined as above has an x-axis unit vector given by the first row. Since the x-axes in the telescope and instrument systems are their boresights, and given the definition of twist angle above, the corresponding telescope celestial coordinates are

$$\alpha_B = \tan^{-1}\left(\frac{-T_{12}}{T_{13}}\right), \quad \delta_B = \sin^{-1}(T_{11}), \quad \gamma_B = \tan^{-1}\left(\frac{-T_{31}}{T_{21}}\right), \tag{3}$$

where T_{ij} denotes the element of T_C^B in row i and column j. The same relationship between celestial angles and transformation matrix elements applies to the instrument system, where the above inverse trigonometric formulas are obvious in equation (2).

The expressions for the right ascension and twist angle are unusable on either pole, because $\cos\delta_B$ is zero and occurs in both numerators and denominators. At the north pole, $\sin\delta_B = 1$, and elements T_{32} and T_{33} reduce to the cosine and sine, respectively, of the sum of the right ascension and twist angle; at the south pole, $\sin\delta_B = -1$, and these elements reduce to the cosine and sine, respectively, of right ascension minus twist angle,

$$\gamma_B = \tan^{-1}\left(\frac{T_{33}}{T_{32}}\right) - \alpha_B \quad \text{(north pole)}, \quad \gamma_B = \alpha_B - \tan^{-1}\left(\frac{T_{33}}{T_{32}}\right) \quad \text{(south pole)}. \tag{4}$$

Right ascension may be set to an arbitrary value, and the twist angle is then given by equation (4). Since these cases are extremely rare, they are ignored in the computation of the mapping matrix below (see § 3.1). The elements of T_C^B needed are

$$\begin{aligned}
T_{11} &= \cos\theta_1\cos\theta_2\sin\delta_M - \sin\theta_1\cos\gamma_M\cos\delta_M\cos\gamma_I + \cos\gamma_M\cos\delta_M\cos\theta_1\sin\theta_2\sin\gamma_I - \sin\theta_1\sin\gamma_M\cos\delta_M\sin\gamma_I \\
&\quad - \sin\gamma_M\cos\delta_M\cos\theta_1\sin\theta_2\cos\gamma_I, \\
T_{12} &= -\cos\theta_1\cos\theta_2\cos\delta_M\sin\alpha_M - \sin\theta_1\cos\gamma_I\cos\gamma_M\sin\delta_M\sin\alpha_M - \sin\theta_1\cos\gamma_I\sin\gamma_M\cos\alpha_M \\
&\quad + \cos\theta_1\sin\theta_2\sin\gamma_I\cos\gamma_M\sin\delta_M\sin\alpha_M + \cos\theta_1\sin\theta_2\sin\gamma_I\sin\gamma_M\cos\alpha_M - \sin\theta_1\sin\gamma_I\sin\gamma_M\sin\delta_M\sin\alpha_M \\
&\quad + \sin\theta_1\sin\gamma_I\cos\gamma_M\cos\alpha_M - \cos\theta_1\sin\theta_2\cos\gamma_I\sin\gamma_M\sin\delta_M\sin\alpha_M + \cos\theta_1\sin\theta_2\cos\gamma_I\cos\gamma_M\cos\alpha_M,
\end{aligned}$$

$$
\begin{aligned}
T_{13} &= \cos\theta_1 \cos\theta_2 \cos\delta_M \cos\alpha_M + \sin\theta_1 \cos\gamma_I \cos\gamma_M \sin\delta_M \cos\alpha_M - \sin\theta_1 \cos\gamma_I \sin\gamma_M \sin\alpha_M \\
&\quad - \cos\theta_1 \sin\theta_2 \sin\gamma_I \cos\gamma_M \sin\delta_M \cos\alpha_M + \cos\theta_1 \sin\theta_2 \sin\gamma_I \sin\gamma_M \sin\alpha_M + \sin\theta_1 \sin\gamma_I \sin\gamma_M \sin\delta_M \cos\alpha_M \\
&\quad + \sin\theta_1 \sin\gamma_I \cos\gamma_M \sin\alpha_M + \cos\theta_1 \sin\theta_2 \cos\gamma_I \sin\gamma_M \sin\delta_M \cos\alpha_M + \cos\theta_1 \sin\theta_2 \cos\gamma_I \cos\gamma_M \sin\alpha_M, \\
T_{21} &= \sin\theta_1 \cos\theta_2 \sin\delta_M + \cos\gamma_M \cos\delta_M \cos\theta_1 \cos\gamma_I + \cos\gamma_M \cos\delta_M \sin\theta_1 \sin\theta_2 \sin\gamma_I + \sin\gamma_M \cos\delta_M \cos\theta_1 \sin\gamma_I \\
&\quad - \sin\gamma_M \cos\delta_M \sin\theta_1 \sin\theta_2 \cos\gamma_I, \\
T_{31} &= -\sin\theta_2 \sin\delta_M + \cos\theta_2 \sin\gamma_I \cos\gamma_M \cos\delta_M - \cos\theta_2 \cos\gamma_I \sin\gamma_M \cos\delta_M. \qquad (5)
\end{aligned}
$$

2.4. Processing Control Data

Most of the processing control parameters can be ignored for purposes of this discussion, but a few should be mentioned. These are as follows.

$\Delta\delta_p$—Distance from a pole within which certain approximations may not be used.
$\Delta\delta_\gamma$—Distance from a pole within which equation (4) must be used for twist angle.
$\chi^2_{\max}$—Maximum 2-D χ^2 value to retain a measurement.
$Q_{\min}$—Minimum acceptable area in the high-end tail of a χ^2 distribution.
R_α—Error variance growth rate in $\Delta\alpha$ estimates.
R_δ—Error variance growth rate in $\Delta\delta$ estimates.
R_γ—Error variance growth rate in $\Delta\gamma$ estimates.
$\Delta T_{\max}$—Maximum time before first measurement or after last measurement to apply telescope-pointing-history corrections.

The first parameter, which defaults to 0.5°, specifies the region around a pole within which two approximations used to speed up the computations may not be employed: (1) the elements of the mapping matrix defined below may not be interpolated in time but must be evaluated explicitly; (2) simple addition of corrections to angles is not permitted, and a more accurate method using vectors is required. The second parameter defaults to 0.01°, within which $|\sin\delta|$ differs from 1.0 by less than 2 parts in 10^8, while $\cos\delta$ becomes small enough to make equation (4) preferable for computing the twist angle.

The third parameter is used in outlier recognition, and the fourth is used to determine whether the uncertainties have been underestimated and need to be inflated.

The next three parameters are random-walk variance rates, i.e., coefficients which multiply time intervals to obtain variances representing uncertainties appropriate to the use of a measurement at a time other than when the measurement was made. It is known that the offsets estimated by the pointing refinement procedure of Paper I vary stochastically in time because of unmodeled residual effects involving gyro drift and thermal alignment changes, but these variations appear to be sampled by typical measurement frequencies well enough to justify linear interpolation of corrections. Nevertheless, there is some unmodeled drift between measurements, and furthermore, it can happen that a lack of point sources in some images results in interpolation over intervals long enough to erode the plausibility of a given bracketing measurement. The variance growths represent unbiased random walks that model the loss of applicability of a measurement with increasing time from that measurement. Since inverse-variance weighting is used in averaging corrections, relatively remote measurements are weighted less and may contribute essentially nothing to the average. If all measurements are distant from the interpolation point, then only the original BPHF measurement survives the averaging. Typical variance-growth rates for right ascension and declination are on the order of 10^{-3} arcsec^2 s^{-1}. Appendix B discusses the random-walk rate calibration.

The last parameter limits the processing of the portion of the pointing history outside the range over which offset measurements exist. Measurement time tags are actually the centers of exposure time intervals, and therefore, parts of the pointing history before the first exposure time and after the last exposure time are used by the standard data-reduction pipeline in averaging the position coordinates of these exposures, necessitating some extrapolation of offset corrections in the SBPHF. The default value is 250 s, which is adequate to cover most exposure times while avoiding the expenditure of computation time on slews.

3. ALGORITHM

The algorithm involves the following steps. For a given BPHF sample, the pair of bracketing measurements in each channel is used to interpolate angle corrections and uncertainties; no assumption is made regarding simultaneity of measurements across channels, because frequently images in the longer wavelengths fail to have enough point sources to yield offset estimates. In each

channel, within $\Delta T_{\max}$ before the first measurement or after the last measurement, the "bracket" does not enclose the BPHF time, and the interpolation becomes extrapolation.

In this procedure, image corrections are treated as measurements; the original BPHF estimates also qualify as measurements, as do the Euler angles relating the instrument coordinates to the telescope coordinates. In terms of correction values, the BPHF and instrument angles contribute values of zero, but their uncertainties are not zero and must be taken into account. This uses all of the available information, and the inverse-variance weighting limits the influence of highly uncertain image corrections. A Gaussian error model is employed and has been found valid through χ^2 testing, provided correlations are taken into account and most non-Gaussian outliers are identified and excluded from the processing.

The *Spitzer* software also handles numerous housekeeping tasks whose details are not described herein, such as grouping image correction sets belonging to corresponding mosaics, allowing user control over which channels are permitted to contribute information, optional output files for quality assurance, etc. Another simplification herein is to limit the discussion to IRAC data; the software was written to accommodate the scan mirror of the Multiband Imaging Photometer for *Spitzer* (MIPS) instrument, which added four independent variables to the observational model, but image corrections for MIPS scan maps have been found to be statistically insignificant relative to the other uncertainties stemming from the longer wavelengths at which this instrument operates, and so the MIPS components of the model have been zero in all actual utilizations and have been formally omitted in this paper.

For a given channel and BPHF sample time that qualifies for correction, the bracketing measurements in that channel are located, and then the operations described in the following sections are performed. Parameters of the bracketing measurement are denoted by the index i herein, where $i = 1, 2$ for the earlier and later time, respectively.

3.1. The Mapping Matrix

The telescope coordinate dependence on the instrument coordinates and the instrument FOV angles is expressed through the *mapping matrix*, which consists of all the relevant partial derivatives. The mapping matrix is used to connect refinement corrections (and their uncertainties) in the instrument pointing frame to those in the telescope frame. It is an affine transformation used to map the correction vector and covariance matrix discussed in § 3.2 from one functional dependence to another. The mapping matrix can be derived from the well-known chain rule of multivariable calculus. For measurement i, this is

$$M_i = \begin{pmatrix} \frac{\partial \alpha_B}{\partial \alpha_M} & \frac{\partial \alpha_B}{\partial \delta_M} & \frac{\partial \alpha_B}{\partial \gamma_M} & \frac{\partial \alpha_B}{\partial \theta_1} & \frac{\partial \alpha_B}{\partial \theta_2} & \frac{\partial \alpha_B}{\partial \gamma_I} \\ \frac{\partial \delta_B}{\partial \alpha_M} & \frac{\partial \delta_B}{\partial \delta_M} & \frac{\partial \delta_B}{\partial \gamma_M} & \frac{\partial \delta_B}{\partial \theta_1} & \frac{\partial \delta_B}{\partial \theta_2} & \frac{\partial \delta_B}{\partial \gamma_I} \\ \frac{\partial \gamma_B}{\partial \alpha_M} & \frac{\partial \gamma_B}{\partial \delta_M} & \frac{\partial \gamma_B}{\partial \gamma_M} & \frac{\partial \gamma_B}{\partial \theta_1} & \frac{\partial \gamma_B}{\partial \theta_2} & \frac{\partial \gamma_B}{\partial \gamma_I} \end{pmatrix}_i, \tag{6}$$

where the subscript i on the matrix indicates that the measurement parameters in the matrix refer to measurement i. The partial derivatives may be obtained from equations (3) and (5). These expressions are generally quite lengthy and are omitted herein.[4]

3.2. The Correction Vectors and Error Covariance Matrices

Corrections in the refined pointing measurement data must be interpolated to individual BPHF sample times. This is done by representing each set of corrections as a vector with associated uncertainties. For the ith record defined in § 2.2, a correction vector is defined as

$$D_i \equiv (\Delta\alpha_M,\ \Delta\delta_M,\ \Delta\gamma_M,\ \Delta\theta_1,\ \Delta\theta_2,\ \Delta\gamma_I)_i, \tag{7}$$

where the last three parameters are corrections to the instrument angles for the channel to which this measurement belongs. These

[4] The partial derivatives may be obtained if desired from the online document http://spider.ipac.caltech.edu/staff/laher/sirtf/Derivatives.pdf.

are set to zero, because no new measurements exist, and so

$$D_i = (\Delta\alpha_M,\ \Delta\delta_M,\ \Delta\gamma_M,\ 0,\ 0,\ 0)_i. \tag{8}$$

The corresponding error covariance matrix is

$$\Omega_i = \begin{pmatrix} V_{\alpha_M} & V_{\alpha\delta_M} & 0 & 0 & 0 & 0 \\ V_{\alpha\delta_M} & V_{\delta_M} & 0 & 0 & 0 & 0 \\ 0 & 0 & V_{\gamma_M} & 0 & 0 & 0 \\ 0 & 0 & 0 & V_{\theta_1} & V_{\theta_1\theta_2} & 0 \\ 0 & 0 & 0 & V_{\theta_1\theta_2} & V_{\theta_2} & 0 \\ 0 & 0 & 0 & 0 & 0 & V_{\gamma_I} \end{pmatrix}_i, \tag{9}$$

where

$$V_{\alpha_M} \equiv \sigma^2_{\alpha_M},\quad V_{\delta_M} \equiv \sigma^2_{\delta_M},\quad V_{\alpha\delta_M} \equiv \sigma_{\alpha\delta_M}\left|\sigma_{\alpha\delta_M}\right|,\quad V_{\gamma_M} \equiv \sigma^2_{\gamma_M},\quad V_{\theta_1} \equiv \sigma^2_{\theta_1},\quad V_{\theta_2} \equiv \sigma^2_{\theta_2},\quad V_{\theta_1\theta_2} \equiv \sigma_{\theta_1\theta_2}\left|\sigma_{\theta_1\theta_2}\right|,\quad V_{\gamma_I} \equiv \sigma^2_{\gamma_I}. \tag{10}$$

3.3. Interpolation

The image correction vectors given in equation (8) are interpolated linearly to the BPHF sample time T_B,

$$\lambda \equiv \frac{T_B - T_{M_1}}{T_{M_2} - T_{M_1}},\quad D = D_1 + \lambda(D_2 - D_1). \tag{11}$$

The first three diagonal elements of the error covariance matrices given in equation (10) are interpolated as described in Appendix A, i.e., approximating the correlation as 100%. For example, interpolation of the first element is performed as

$$V_{\alpha_M} = \left[(1-\lambda)\sigma_{\alpha_{M_1}} + \lambda\sigma_{\alpha_{M_2}}\right]^2. \tag{12}$$

The instrument angle uncertainties are constants and need no interpolation. The covariance element for right ascension and declination is interpolated approximately via the correlation coefficient:

$$\rho_i \equiv \left(\frac{V_{\alpha\delta_M}}{\sqrt{V_{\alpha_M}V_{\delta_M}}}\right)_i,\quad i = 1,\ 2,\quad \rho = \rho_1 + \lambda(\rho_2 - \rho_1),\quad V_{\alpha\delta_M} = \rho\sqrt{V_{\alpha_M}V_{\delta_M}}, \tag{13}$$

where the quantities on the right-hand side of the last equation of the line are all interpolated values. The exact expression depends on correlations between all combinations of right ascension and declination measurement errors at both bracket times, but except for the correlations taken into account above, these other correlations were found to be generally quite small in Paper I and are not retained in the production processing mode. The important error correlations are (1) across time for corrections in each angle and (2) between right ascension and declination at each measurement. The former tend to be quite strong, while the latter do not but are occasionally significant enough to be taken into account in an approximate manner. The assumption that this correlation varies approximately linearly from one measurement to the next appears reasonable.

The random-walk component of uncertainty in the right ascension correction is computed in a standard forward-backward smoothing manner which goes to zero at measurement times but supplies appropriate additional uncertainty in between,

$$V_{R_{\alpha_i}} = R_\alpha|T_i - T_B|,\quad i = 1,\ 2,\quad V_{R_\alpha} = \frac{V_{R_{\alpha1}}V_{R_{\alpha2}}}{V_{R_{\alpha1}} + V_{R_{\alpha2}}} = \lambda(1-\lambda)R_\alpha(T_2 - T_1). \tag{14}$$

The declination and twist random-walk terms are computed similarly, and then each is added to its corresponding diagonal element in the interpolated error covariance matrix, for which the final result is denoted Ω_M. The mapping matrix elements are also interpolated linearly except in the vicinity of a pole, wherein the formal expressions are evaluated explicitly for linearly interpolated values of the refined measurement right ascension, declination, and twist. In practice, the unit-vector axes of the measurement coordinate system are interpolated, and the angles are extracted via equations (3) or (4). The interpolated mapping matrix is denoted M.

3.4. Mapping to the Telescope System

The interpolated correction vector is mapped to the telescope coordinate system as follows, where the superscript T indicates that the vector is transposed, and again, the subscript B stands for BPHF and corresponds to the telescope coordinate system,

$$D_B \equiv \begin{pmatrix} \Delta\alpha_B \\ \Delta\delta_B \\ \Delta\gamma_B \end{pmatrix} = MD^T. \tag{15}$$

The corresponding error covariance matrix is

$$\Omega_B = M\Omega_M M^T. \tag{16}$$

Note that because the mapping matrix contains three rows and six columns, the correction vector and the error covariance matrix are mapped down from six dimensions to three: right ascension, declination, and twist. Equation (16) is a standard operation in optimal filtering theory, whereas equation (15) amounts to a Taylor's expansion in which terms above first order are dropped, because the increments mapped are later added (generally after some averaging) to (α_B, δ_B, γ_B), which are treated here as functions of (α_M, δ_M, γ_M, θ_1, θ_2, γ_I). In other words, the vector ($\alpha_B + \Delta\alpha_B$, $\delta_B + \Delta\delta_B$, $\gamma_B + \Delta\gamma_B$) is a linearized approximation to a function of ($\alpha_M + \Delta\alpha_M$, $\delta_M + \Delta\delta_M$, $\gamma_M + \Delta\gamma_M$, θ_1, θ_2, γ_I). The accuracy of this approximation was examined for realistic correction values over a large sample of sky locations and orientations. The approximation errors in telescope boresight direction were always found to amount to less than 40 microarcseconds (μas) except within 2° of a pole; at 1° from a pole, the maximum error was 1 mas. More than 10° from a pole, the error was always less than 1 μas. The approximation error in linearly interpolating the mapping matrix (or near a pole, interpolating the angles defining it) was similarly examined and found never to exceed 0.1 mas for typical interpolation intervals, with the error always dominated by the random-walk uncertainty.

3.5. Outlier Detection

The correction vector and error covariance matrix represented in the telescope system as shown in equations (15) and (16) respectively are derived from a single IRAC channel. In principle up to four channels are available. The vectors and matrices for each measurement will be indicated by a subscript k, which runs from 1 to N, i.e., D_{Bk} and Ω_{Bk}, respectively, where N is the total number of measurements available. In addition, the original BPHF sample, with its implicit null correction vector and its own error covariance matrix, constitutes a measurement which will be indicated by a value of $k = 0$, i.e.,

$$D_{B_0} = \begin{pmatrix} 0 \\ 0 \\ 0 \end{pmatrix}, \quad \Omega_{B_0} = \begin{pmatrix} V_{\alpha_B} & V_{\alpha\delta_B} & 0 \\ V_{\alpha\delta_B} & V_{\delta_B} & 0 \\ 0 & 0 & V_{\gamma_B} \end{pmatrix}, \quad V_{\alpha_B} \equiv \sigma^2_{\alpha_B}, \quad V_{\delta_B} \equiv \sigma^2_{\delta_B}, \quad V_{\alpha\delta_B} \equiv \sigma_{\alpha\delta_B}\left|\sigma_{\alpha\delta_B}\right|, \quad V_{\gamma_B} \equiv \sigma^2_{\gamma_B}. \tag{17}$$

Discordant measurements are always a concern in any nontrivial averaging process. One of the great advantages of having prior error statistics is that plausibility tests can be performed, and outliers can be kept out of the average. In this case, all combinations of pairwise measurements are compared to see whether the differences are reasonable given the expected discrepancy level described by the uncertainties. This is accomplished via a two-dimensional χ^2 test. Given the twist angle's relatively higher uncertainties and lesser impact, the possibility of diluting the test by including it in the χ^2 is eliminated by testing only right ascension and declination. The χ^2 for the two measurements in which the index k takes on the two values m and n is

$$d_{mn} \equiv (\Delta\alpha_{B_m} - \Delta\alpha_{B_n},\ \Delta\delta_{B_m} - \Delta\delta_{B_n}), \quad \Omega_{mn} \equiv \begin{pmatrix} V_{\alpha B_m} + V_{\alpha B_n} & V_{\alpha\delta B_m} + V_{\alpha\delta B_n} \\ V_{\alpha\delta B_m} + V_{\alpha\delta B_n} & V_{\delta B_m} + V_{\delta B_n} \end{pmatrix}, \quad \chi^2_{mn} = \chi^2_{nm} = d_{mn}\Omega^{-1}_{mn}d^T_{mn}. \tag{18}$$

If $\chi^2_{mn} > \chi^2_{\max}$, then either measurement m or measurement n must be rejected. The original BPHF measurements are never rejected, however, so if $m = 0$, then n is rejected, and vice versa. If neither measurement is the BPHF, then

$$S_m \equiv \sum_{i \neq m,n} \chi^2_{im}, \quad S_n \equiv \sum_{i \neq m,n} \chi^2_{in}. \tag{19}$$

If $S_m > S_n$, then measurement m is rejected, otherwise measurement n is rejected. This process is repeated until no χ^2 are found to be above the maximum permitted. The default value for $\chi^2_{\max}$ is 18.42, so if the error statistics were perfect and there were no glitches, about 1 out of every 10,000 measurement pairs would trigger rejection processing. This threshold was set by varying it and visually determining whether the rejected measurements were outliers. In practice, measurements are typically rejected at a

rate of just under 1%, but these are almost exclusively in IRAC channels 3 and 4, where sparser measurements cause longer interpolation intervals that suffer more from random walk than measurements in channels 1 and 2, which are almost never rejected. The distribution of outliers over time is quite nonuniform, with some BPHF 12 hr periods having no diagnosed outliers at all.

3.6. Averaging Multiple-Channel Measurements

The averaged correction vector and its error covariance matrix are obtained via standard Gaussian estimation,

$$\Omega_{\rm avg} = \left(\sum_{k=0}^{N} \Omega_{B_k}^{-1}\right)^{-1}, \quad D_{\rm avg} = \Omega \sum_{k=0}^{N} \Omega_{B_k}^{-1} D_{B_k}. \tag{20}$$

3.7. Applying the Corrections

Outside of the radial distance $\Delta\delta_p$ from a pole, the corrections given by equation (20) are simply added to the corresponding BPHF coordinate angles; within that distance of a pole, the corrections are used as differential elements in the total derivatives of the elements of T_C^B to compute increments that are added to the corresponding elements as

$$V_{ij} \equiv \left(\frac{\partial T_{ij}}{\partial \alpha_B}, \frac{\partial T_{ij}}{\partial \delta_B}, \frac{\partial T_{ij}}{\partial \gamma_B}\right), \quad \Delta T_{ij} = V_{ij} D_{\rm avg}, \quad T_{ij} \leftarrow T_{ij} + \Delta T_{ij}. \tag{21}$$

The SBPHF right ascension, declination, and twist are then obtained by using the modified matrix elements in equations (3) and (4) after first enforcing the orthonormality of the matrix (see Appendix C). This method of applying the corrections can be used anywhere on the sky, but because it is computationally expensive compared to simple addition of the corrections, it is used only near poles in practice. The error covariance matrix in equation (20) supplies the uncertainties for the SBPHF angles for both methods.

3.8. Uncertainty Inflation

The final step in preparing each SBPHF sample is to verify that the right ascension and declination uncertainties are plausible in the context of the prior uncertainties and observed dispersion about the average. Again a χ^2 test is employed. The processing for right ascension will be described; declination and twist are handled similarly. The top left element of each of the Ω_{B_k} error covariance matrices is the variance for uncertainty in right ascension; this will be denoted V_{α_k}. The first element of each correction vector is the value for right ascension and will be denoted $\Delta\alpha_k$. The average correction obtained via equation (20) is denoted $\Delta\alpha$ with uncertainty variance V_α. Then the χ^2 parameter is

$$\chi_N^2 = \sum_{k=0}^{N} \frac{(\Delta\alpha_k - \Delta\alpha)^2}{V_{\alpha_k} + V_\alpha}. \tag{22}$$

Note that there are $N + 1$ measurements included in the χ^2 summation because k runs from 0 to N; the number of degrees of freedom is one less because of the use of the average correction in each numerator. If $Q_N(\chi_N^2) < Q_{\rm min}$, where $Q_N(\chi_N^2)$ is the area beyond χ_N^2 under the high tail of a χ^2 distribution with N degrees of freedom, then the uncertainty in right ascension is taken to be underestimated and is inflated as follows,

$$V_\alpha \leftarrow V_\alpha \frac{\chi_N^2}{N}. \tag{23}$$

This adjustment is based on the assumption that all input uncertainties in right ascension were underestimated by the same scale factor, causing the high value for χ^2; if all the right ascension error variances were scaled as shown in equation (23), then equation (20) would yield the same average correction for this angle, but the uncertainty would be that on the left-hand side of equation (23), and the χ^2 value of equation (22) would be equal to the number of degrees of freedom. The default value for $Q_{\rm min}$ is 0.001, so if all error statistics were perfect, one result out of every thousand would trigger the adjustment. In practice, about 0.56% of all output uncertainties are adjusted, of which 75% are for declination. The time distribution of measurements requiring uncertainty inflation is quite nonuniform, similar to that for outlier detection.

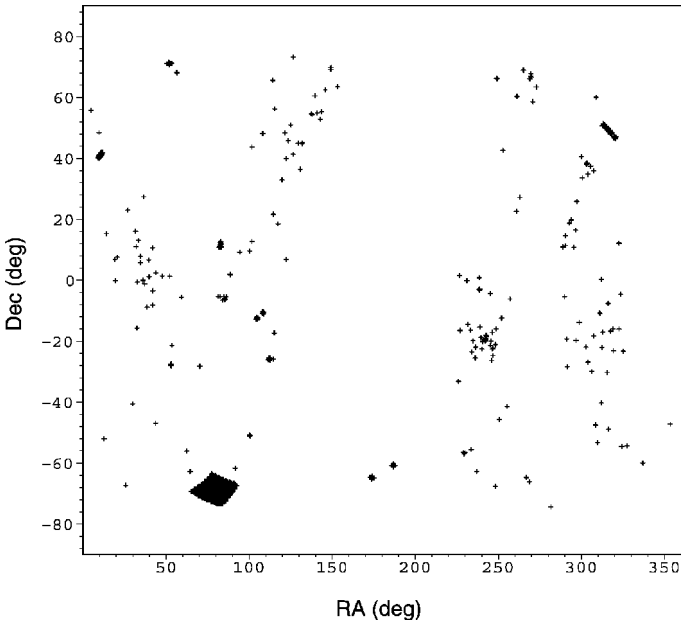

Fig. 2.—Sky distribution of IRAC observations in the test suite.

4. DISCUSSION AND CONCLUSIONS

The 86,401 samples of pointing information in a BPHF are each processed as described in § 3, and a new file, the SBPHF, is written that contains the refined pointing information. This file is named according to a convention different from that of the BPHF but may be used instead of the BPHF by any *Spitzer* data-analysis software. Since some samples cannot be processed, those which are modified are tagged in a field of the record not otherwise used. This permits backward compatibility while enabling any future need for automated distinction between BPHF and SBPHF information.

Right ascension and declination uncertainties in a BPHF are typically about 1″; this typically drops to about 0.07 in the SBPHF, which is also the typical midinterpolation value of the random walk uncertainties. The pointing correction uncertainties are typically on the order of several hundredths of an arcsecond, so samples in between measurements are dominated by the random-walk uncertainty. Typical correction magnitudes are several tenths of an arcsecond. Mosaics created from images whose positions were computed from the SBPHF demonstrate the improvements over those based on the BPHF, the same improvements as those shown in Paper I.

These aspects of the SBPHF results were observed primarily by examining the results from a test suite of data taken between 2005 August 18 and November 2. The numbers of correction records (as described in § 2.2) in IRAC channels 1 through 4 are 37,836, 37,717, 33,209, and 35,085, respectively. The distribution of observations over the entire sky is shown in Figure 2 as a Cartesian plot in right ascension and declination (the large mosaic in the south is a mapping of the Large Magellanic Cloud). Histograms of corrections in the three angles for the four channels are shown in Figure 3; each histogram is shown with a superposed Gaussian distribution with the same mean and standard deviation. The main statistical parameters of each histogram are summarized in Table 2, where the skewness and excess kurtosis confirm the deviations from a Gaussian distribution seen in Figure 3. These deviations have been shown to result from mixing several different Gaussian populations that result from a single Gaussian population on each instrument array axis being mapped through a nonuniform distribution of twist angles onto the sky. For IRAC channels 1 and 2, which dominate the processing, the distribution of pointing errors on each instrument coordinate axis has very low skewness and excess kurtosis, but the *y*-axes (as defined in Paper I) have statistically very significant nonzero means between 0.25″ and 0.3″. The coupling of these nonzero means into celestial coordinates depends on the twist, which is nonuniformly distributed because of spacecraft sunshade constraints. The statistical emergence of the nonzero mean pointing errors is a by-product of the processing described in Paper I and could be used to refine the FOV angles if desired, but the overhead of bookkeeping a time dependence in the FOV values exceeds any benefits, since these offsets are removed effectively by the processing described herein.

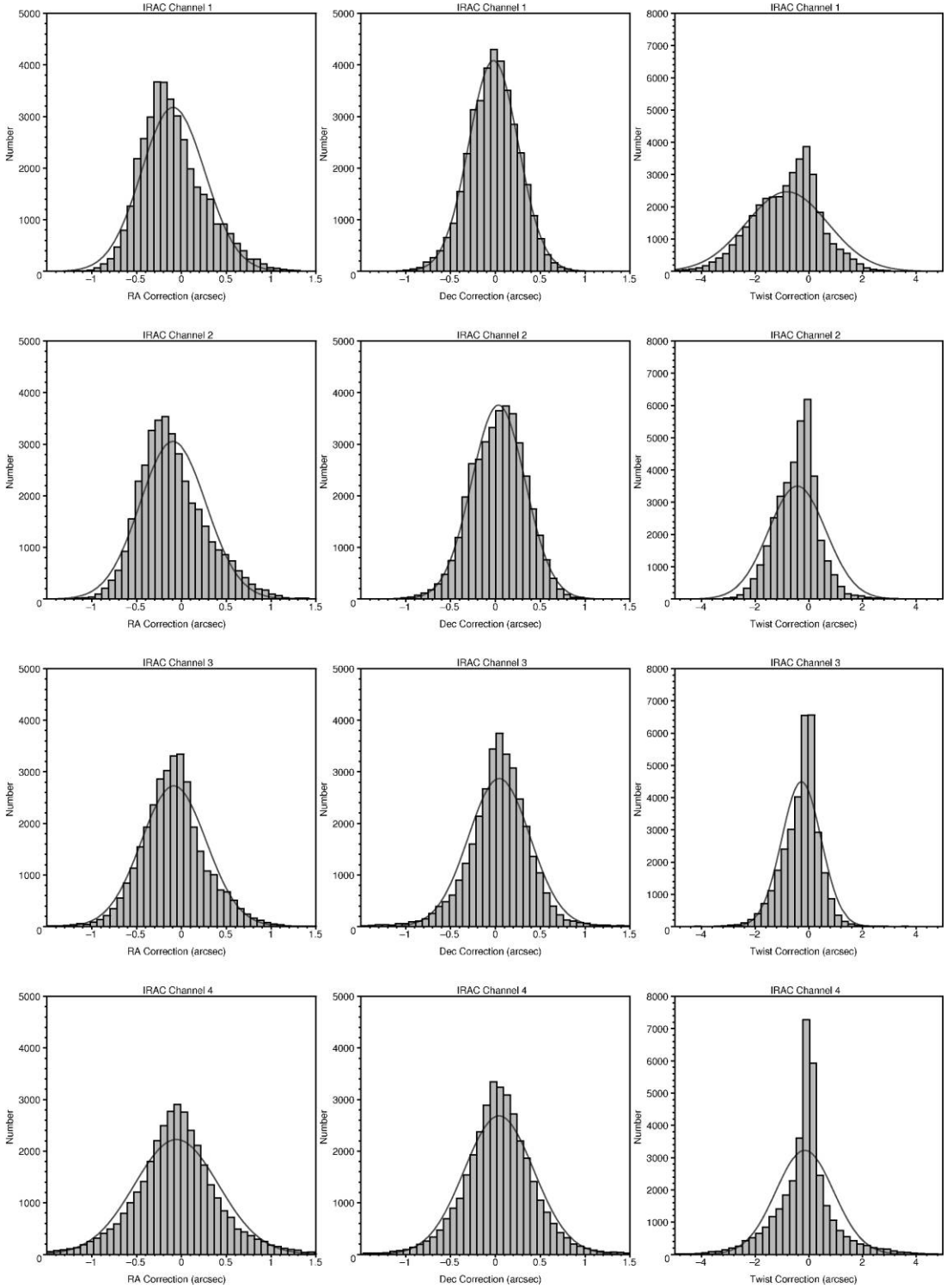

FIG. 3.—Histograms of corrections to R.A., decl., and twist in the four IRAC channels. Superposed Gaussians have the same mean and standard deviation as the histogram.

TABLE 2
STATISTICAL PARAMETER VALUES FOR THE ANGLE CORRECTIONS

IRAC Channel	Angle	Mean (arcsec)	Std. Dev. (arcsec)	Median (arcsec)	Mode (arcsec)	Minimum (arcsec)	Maximum (arcsec)	1% (arcsec)	99% (arcsec)	Skewness	Excess Kurtosis
1	R.A.	−0.093	0.355	−0.142	−0.251	−1.567	1.322	−0.784	0.873	0.584	0.371
	Decl.	−0.021	0.276	−0.017	0.153	−2.147	1.068	−0.711	0.602	−0.139	0.301
	Twist	−0.813	1.522	−0.668	−0.124	−57.642	37.488	−3.924	1.919	−1.943	149.196
2	R.A.	−0.095	0.368	−0.145	0.000	−1.335	1.419	−0.815	0.909	0.587	0.345
	Decl.	0.034	0.299	0.046	0.000	−2.187	1.062	−0.701	0.677	−0.196	0.129
	Twist	−0.431	1.069	−0.354	−0.100	−36.716	29.610	−2.319	1.626	−3.245	292.958
3	R.A.	−0.085	0.362	−0.093	−0.065	−2.134	2.333	−0.941	0.860	0.226	1.947
	Decl.	0.043	0.344	0.051	0.011	−2.686	2.776	−0.927	0.911	−0.162	3.052
	Twist	−0.275	0.733	−0.163	−0.004	−7.006	8.442	−2.242	1.270	−0.157	11.519
4	R.A.	−0.056	0.469	−0.057	0.000	−2.618	3.422	−1.277	1.199	0.079	1.539
	Decl.	0.040	0.389	0.039	0.000	−2.739	2.249	−0.980	1.060	−0.011	2.064
	Twist	−0.153	1.079	−0.069	−0.055	−7.500	6.308	−3.180	3.065	0.033	3.055

The relationship between the SBPHF solution and the corresponding BPHF solution is illustrated for the right ascension of a randomly selected 60 s IRAC exposure in Figure 4. The BPHF values for right ascension as a function of time are shown as a solid line in the center of the plot. The top and bottom solid lines trace the 1 σ contour about the nominal values. The SBPHF solution is shown in dashed lines, with the center line giving the nominal values, and the top and bottom dashed lines showing the SBPHF 1 σ contour. The SBPHF solution is completely consistent with the BPHF solution, falling well within the latter's 1 σ contour. The reverse is not true, however; from the point of view of the SBPHF, the BPHF is in error with a significance varying between about 2 and 3 σ.

The time variation of the SBPHF uncertainty is shown for the declination of a randomly selected period of 87 s spanning eight IRAC exposures in Figure 5. Each minimum is at a central exposure time. Between minima, the effect of the random-walk uncertainty is seen. The uncertainty varies between 0.0630 and 0.0813″. The BPHF uncertainty during this period is 1.086″, almost 11 times too high to fit in the plot. This gain in accuracy is typical of SBPHF solutions.

This work is based in part on archival data obtained with the *Spitzer Space Telescope*, which is operated by the Jet Propulsion Laboratory, California Institute of Technology under a contract with NASA. Support for this work was provided by an award issued by JPL/Caltech.

APPENDIX A

UNCERTAINTY INTERPOLATION

Paper I presented graphical representations of the correlation coefficients between all fitting parameter uncertainties for a sample mosaic. The actual numerical results show that uncertainties in solutions for corrections in a given channel to a given angle tend to be significantly correlated from one measurement to another. In other words, in the notation of § 2.2, the uncertainty in $\Delta\alpha_M$ for measurement m tends to be significantly correlated with that of $\Delta\alpha_M$ in measurement n, $m \neq n$. The correlation is always positive and typically runs from about 35% in IRAC channel 1 to essentially 100% in IRAC channel 4. It does not tend to fall off significantly with increasing difference between m and n, i.e., chronologically distant measurements tend to be as correlated as adjacent ones.

Significant error correlation is not unusual in parameter-fitting computations; error in one parameter often implies error in the others; hence, they are correlated. As discussed in Paper I, the association of *Spitzer* and 2MASS point sources is performed where possible. The astrometric quality of the 2MASS catalog provides absolute position information which dilutes the error correlation that is induced by *Spitzer*-only point-source tie points between images, whose relative position information is strong but whose absolute position information is somewhat weaker. 2MASS astrometric sources are less commonly observed in the longer wavelengths; hence, the correlations are not alleviated there. This correlated position uncertainty causes an IRAC channel 4 mosaic to be like a fairly rigid body that can be erroneously shifted somewhat as a whole, but whose parts cannot move very much relative to each other. IRAC channel 1 tends to have enough 2MASS astrometric tie points to anchor its mosaics more firmly to absolute position, and this reduces the error correlation noticeably but does not eliminate it.

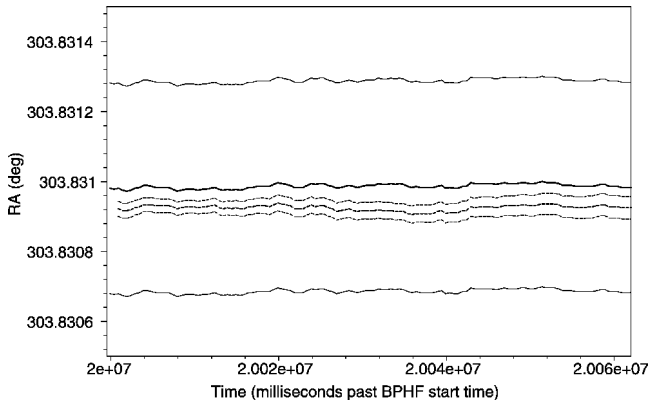

FIG. 4.—BPHF and SBPHF solutions for the same period. The center solid line shows BPHF solution for R.A. vs. time; outer solid lines are the 1 σ contours; the center dashed line is the SBPHF solution, with outer dashed lines showing its 1 σ contour; the SBPHF solution lies well within the BPHF 1 σ contour, but the BPHF solution is significantly outside the SBPHF 1 σ contour.

These correlations affect how the uncertainties are interpolated between measurements. For any one of the three angle corrections, we denote the error in that correction ε, and use the notation of equation (11) along with the fact that linear interpolation of the correction from measurement 1 to measurement 2 amounts to simultaneous linear interpolations of the true value and the error. Then the error in the interpolated correction is

$$\varepsilon = (1 - \lambda)\varepsilon_1 + \lambda\varepsilon_2, \tag{24}$$

where λ is the linear interpolation coefficient defined by equation (11). Squaring this and taking expectation values yields

$$\langle\varepsilon^2\rangle = (1 - \lambda)^2\langle\varepsilon_1^2\rangle + \lambda^2\langle\varepsilon_2^2\rangle + 2\lambda(1 - \lambda)\langle\varepsilon_1\varepsilon_2\rangle, \quad \sigma^2 = (1 - \lambda)^2\sigma_1^2 + \lambda^2\sigma_2^2 + 2\lambda(1 - \lambda)\rho_{12}\sigma_1\sigma_2, \tag{25}$$

where the correlation coefficient for the errors in this correction at measurements 1 and 2 is

$$\rho_{12} = \frac{\langle\varepsilon_1\varepsilon_2\rangle}{\sigma_1\sigma_2}. \tag{26}$$

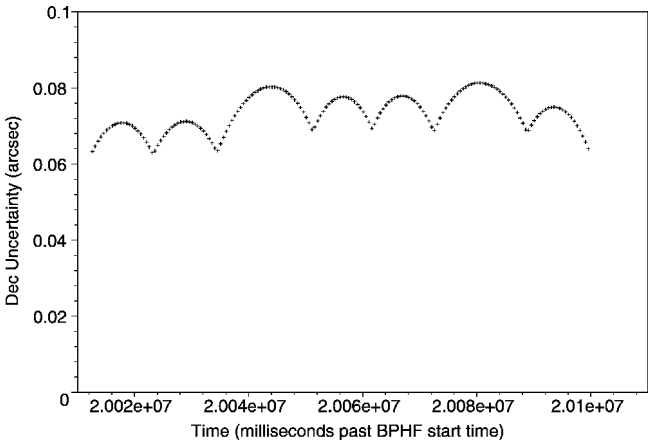

FIG. 5.—SBPHF decl. uncertainty over a span of eight IRAC exposures. The time spanned by the samples is 87 s; the BPHF uncertainty is a constant 1.086″ during this period, almost 11 times greater than the upper limit of the plot.

For uncorrelated errors, $\rho_{12} = 0$, eliminating the last term in the second line of equation (25). For 100% correlation, $\rho_{12} = 1$, and that equation can be simply factored back into

$$\sigma^2 = [(1 - \lambda)\sigma_1 + \lambda\sigma_2]^2. \tag{27}$$

Since ρ_{12} is the only variable in the second line of equation (25) that can be negative, for $\lambda \neq 0$ or 1, any value of ρ_{12} less than 1 reduces the interpolated uncertainty variance, and so equation (27) yields the maximal value. This is very close to the correct value in the longer wavelengths and somewhat of an overestimate in the shorter wavelengths. It is used for all wavelengths, because the overestimation occurs well inside the interpolation interval, where the uncertainty due to random walk tends to dominate anyway.

APPENDIX B

RANDOM WALK CALIBRATION

Equation (14) shows the computation of the uncertainty in right ascension due to random walk from a linear path between measurements. For each angle, the random walk is described by a single parameter whose value must be obtained through calibration. The linear interpolation of corrections is justified on the basis that the pointing error in the BPHF drifts slowly enough so that the measurement frequency samples the error well enough to allow approximating the changes between measurements as linear. In other words, the typical deviation from linearity is claimed to be relatively small compared to the correction itself. This has been checked by computing the power spectrum and autocorrelation function for the corrections obtained from hundreds of mosaics. The power spectra typically vary as $1/f^{0.8}$ with variations of ± 0.1 in the exponent, and the autocorrelation between successive samples is typically about 0.7, falling to 0.1 after several hundred measurements, and approaching zero after several thousand. We conclude that linear interpolation captures most of the correction but leaves enough error to require accounting in the uncertainty as random walk.

Since the autocorrelation drops off rather slowly for nearly adjacent measurements, we assume that partitioning the measurements by separating the even-numbered ones from the odd-numbered ones would result in slightly higher random-walk error but not overwhelmingly so. This allows us to use the odd-numbered measurements as the "measurements" and to take the even-numbered ones as samples of the random drift between "measurements." Computing the statistics of these random drifts should yield a slightly conservative estimate of the random walk between the actual measurements, and the calibration implements this idea.

The calibration method is the same for right ascension, declination, and twist, so we will describe the procedure generically. We compute the linear trajectory of the correction between measurement n and $n + 2$, and we take measurement $n + 1$ as a sample of random walk from linearity, denoting the difference between it and the linear trajectory Δx. We form the sum

$$S = \sum [\Delta x^2 - \lambda(1 - \lambda)\Delta TR]^2 \tag{28}$$

over all Δx-values, where ΔT is $T_{n+2} - T_n$, and $\lambda = (T_{n+1} - T_n)/\Delta T$. Note that this ascribes all of Δx to random walk, ignoring the contribution of the errors at each of the three measurements; this is justified on the basis of the fact that the measurement errors are typically 2 orders or magnitude smaller than the midinterpolation random-walk excursions. The derivative of S with respect to R is set to zero, and the resulting equation is solved for R to obtain the random-walk coefficient. This procedure yielded very close results for right ascension and declination in IRAC channels 1 and 2, about 0.0012 arcsec^2 s^{-1}. Larger values were obtained in channels 3 and 4 but were rejected because of the greater measurement errors therein and the fact that the random walk is a property of the telescope and its pointing reconstruction and therefore must be the same in all channels. As expected, the random-walk rate for twist was larger, with a value of 0.0320 arcsec^2 s^{-1}.

APPENDIX C

RESTORING ORTHONORMALITY TO THE TRANSFORMATION MATRIX

Equation (21) shows how corrections are applied in the vicinity of a pole, where simple addition of corrections to the corresponding angles can cause problems like shifting the pointing over the pole, and the interpretation of an azimuthal angular interval in right ascension becomes very dependent on the accompanying declination. To avoid such problems, the elements of the transformation

matrix itself are modified via exact dependence on the angle corrections, which are always small enough to treat as differential increments. However, round-off errors involved in operating directly on the matrix elements can leave the matrix in a nonorthonormal state, at least in principle. Since the final attitude angles are extracted from the matrix via equations (3) and (4), it is important that the matrix be orthonormal. In practice, only negligible errors have been found when all computations are done in double precision, and the context is not one in which errors are propagated and would accumulate, but prudence dictates repairing potential drift from orthonormality in general. The interpolation of coordinate system axes mentioned in § 3.3 also does not generally preserve orthonormality, and so the procedure described in this appendix is also applied after that processing.

On the other hand, imposing orthonormality on a nonorthonormal matrix is a problem with no unique solution. To see this, consider two distinct orthonormal matrices M_1 and M_2 and one nonorthonormal matrix M_3. Both M_1 and M_2 can be rescaled on an element-by-element basis to make them equal to M_3. The task of enforcing orthonormality in M_3 then clearly suffers from ambiguity in whether the result should be M_1 or M_2 or any other of the infinite number of orthonormal matrices.

Another way to view the dilemma is to observe that a three-dimensional matrix contains nine elements, whereas the number of orthonormality constraints is 12, i.e., three unit rows, three unit columns, null dot products between the three pairs of rows, and null dot products between the three pairs of columns. The unit-magnitude constraints are not linearly independent. Any nonsingular three-dimensional matrix could be made orthonormal by a set of nine scale factors, but the system of equations based on any linearly independent subset of the orthonormality constraints is nonlinear in the scale factors, and its solution is not unique in general.

Intuitively it is obvious, however, that some orthonormal matrix very close to the one resulting from equation (21) must be the right answer, and various approaches to restoring orthonormality via minimization of some cost function are possible. Here we assume that deviations from orthonormality are small and that the right answer lies between what we obtain via row normalization and column normalization.

We use the fact that for any three-dimensional orthonormal matrix, there exists a yaw-roll-yaw Euler angle set that will yield that matrix. The *Spitzer* rotation conventions described in § 2.2 ($\alpha_M - 90°$ about X, $\delta_M - 90°$ about Z, and γ_M about X) are such a set and will suffice for present purposes. Therefore, after applying equation (21), the method for enforcing orthonormality is as follows: (1) unit normalize the rows of the matrix and extract the three angles via equations (3) or (4) as appropriate; (2) independently unit normalize the columns and extract another set of the three angles; (3) average the corresponding angles from each set (taking the usual care at azimuthal-angle zero points); and (4) construct the matrix from the averaged angles according to equation (2). This manner of constructing the matrix guarantees its orthonormality. Since its yaw-roll-yaw angles are the average of the results for two independent approximate normalizations, they should generally lie sufficiently close to the "correct" answer, whose existence intuition demands. In the present case, they are the angles sought, and the actual construction of the matrix is unnecessary unless needed for other purposes.

Another approach that was investigated is based on the fact that for an orthonormal matrix, the inverse and transpose are equal. Any differences are removed iteratively by averaging the inverse and the transpose. Given a matrix M, we attach a subscript zero to indicate its state after computations that may have left it nonorthonormal. The average of the inverse and the transpose at the state with subscript n should be a better estimate of both the inverse and the transpose at the state with subscript $n + 1$. Since it is unclear whether this average should be inverted or transposed to recover the next estimate of the matrix, we do both and average the result,

$$M_{n+1} = \frac{(M_n^T + M_n^{-1})^T/2 + (M_n^T + M_n^{-1})^{-1}/2}{2} = \frac{2M_n + (M_n^{-1})^T + (M_n^T)^{-1}}{4}. \tag{29}$$

This recursive expression is iterated until the deviations from the orthonormality constraints drop below a chosen threshold. The iteration was found to converge rapidly, even for initial large deviations from orthonormality. The first method was chosen because it does not require iteration.

Tests of these methods on matrices whose orthonormality was corrupted with small pseudorandom perturbations showed that their results are better than the corrupted matrix but are not panaceas for information lost to round-off error. Comparing angles extracted from the corrupted matrix to those extracted from the reorthonormalized one using either method showed that both have zero-mean errors with standard deviations about 20% smaller for the latter. The two methods performed equally well but provided slightly different answers in general. Because the error dispersion was reduced compared to the corrupted matrix, we conclude that the procedure is worthwhile, especially when the matrix is needed for subsequent transformations whose results would be degraded by any significant lack of orthonormality. In the present case, given the small size of the round-off errors expected in the application of equation (21), these effects on the matrix and its associated angles should have an accuracy impact orders of magnitude smaller than the *Spitzer* requirements.

REFERENCES

Bayard, D. S., Ahmed, A., & Brugarolas, P. B. 2003, JPL, D-24808
Laher, R., McCallon, H., Masci, F., & Fowler, J. 2006, ASP Conf. Ser. 351, Astronomical Data Analysis Software and Systems XV, ed. C. Gabriel et al. (San Francisco: ASP), 169
Masci, F. J., Makovoz, D., & Moshir, M. 2004, PASP, 116, 842 (Paper I)
Skrutskie, M. F., et al. 2006, AJ, 131, 1163
Werner, M. W., Roellig, T. L., Low, F. J., et al. 2004, ApJS, 154, 1